Experimental and numerical investigation of two flame stabilization regimes observed in a dual swirl H2-air coaxial injecto

Andrea Aniello, Davide Laera, Sylvain Marragou, Hervé Magnes, Laurent Selle, Thierry Schuller, Thierry Poinsot

Experimental and numerical investigation of two flame stabilization regimes observed in a dual swirl H_2-air coaxial injector

A. Aniello[a,*], D. Laera[b,c], S. Marragou[a], H. Magnes[a], L. Selle[a], T. Schuller[a], T. Poinsot[a]

[a] *Institut de Mécanique des Fluides de Toulouse, IMFT, Université de Toulouse, CNRS, 31400 Toulouse, France*
[b] *CERFACS, 42 avenue Gaspard Coriolis, 31057 Toulouse, France*
[c] *Department of Mechanics, Mathematics and Management - Polythechnic of Bari, Via Re David, 200, 70125 Bari, Italy*

Abstract

This study investigates H_2-air flames obtained with a laboratory scale coaxial dual-swirl injector in which fuel and oxidizer are injected separately. Two flame archetypes are observed experimentally for the same global equivalence ratio $\phi_g \approx 0.45$ and two different thermal powers: a flame anchored to the injector ($\approx$ 4 kW) and an aerodynamically stabilized flame exhibiting a characteristic V-shape ($\approx$ 10 kW). Large Eddy Simulations (LES) allow to retrieve both regimes and are used to investigate these two stabilization modes. The numerical setup is first validated against isothermal and reactive Particle Image Velocimetry measurements and OH^* chemiluminescence images. The mean velocity field of both operating conditions reveals the existence of a strong inner recirculation zone (IRZ) that, penetrating inside the injector nozzles, leads to a radial divergence of the central hydrogen jet, which ultimately favors one stabilization regime over the other. The first flame anchors on the hydrogen injector lip and it develops along the mixing layer between H_2 and air swirling jets. The lifted flame, instead, stabilizes in the inner shear layer between the IRZ and the exiting swirling jet of fresh gases, burning over a wide range of equivalence ratios. LES also unveils the flame structures typical of each flame: the anchored one is entirely controlled by diffusion, while the lifted flame is characterized by a first partially premixed branch and a second diffusion front. Finally, high-speed camera and LES are used to analyze the unsteady transition from lifted to anchored flames.

Keywords: H_2 swirling flames, Large Eddy Simulation, Flame stabilization, Premixed flame, Diffusion flame

*Corresponding author: andrea.aniello@imft.fr

1. Introduction

Green H_2 is a promising fuel to decarbonize the combustion processes and ensure the transition towards renewable energy carriers. Hydrogen can be produced via electrolysis using green-electricity, favoring the abatement of both direct and indirect CO_2 emissions that are inherent to fossil fuels. However, most of existing technologies cannot sustain full H_2 operations [1, 2, 3] because of its atypical combustion properties [4]. Hydrogen is characterized by a larger laminar burning velocity [5, 6, 7], higher molecular diffusion [8] and lower activation energy [4] than common hydrocarbons. These properties can affect the flame shape and the stabilization mode with direct consequences on combustion efficiency and pollutant emissions. In premixed systems it also increases the risk of spontaneous ignition [9, 10] or flashback [11, 12]. To avoid these problems, separated injection of reactants is generally preferred. This, however, leads to non-premixed flames, whose stabilization represents a classical problem for the combustion community [13, 14].

Pioneering works on turbulent jet diffusion flames assumed that the flame leading point burns in perfectly premixed mode at stoichiometric conditions [15] or along the mixture fraction corresponding to the maximum laminar burning velocity [16]. Other studies justify instead the transition from anchored to lifted flame by local flame extinction [17, 18]. More recent work on CH_4-air jet diffusion flames exploits cinema-PIV for Reynolds numbers up to $Re = 8500$ to analyze the dynamics of the flame leading edge considering both the local turbulent intensity and the passage of large vortical structures through the flame zone [19]. This study does not show a strict correlation between the flame position and the turbulent vortices, but it reveals a divergence of the streamlines upstream of the flame that is compatible with the concept of triple flame. The deceleration of the flow in front of the triple flame leading edge is due to the gas expansion over the non-flat flame surface and facilitates flame stabilization in high velocity flows, as demonstrated by theory [20]. This result corroborates previous studies on CH_4-air mixtures [21, 22], which identify triple flame propagation as the main mechanism for turbulent jet diffusion flame stabilization. The impact of the degree of mixing on the lift-off height in jet diffusion flames was also investigated [23, 24].

When swirling flows are considered, additional phenomena must be taken into account [25]. First, an Inner Recirculation Zone (IRZ) of hot gases enhances flame stabilization, which serves as a source of energy for the incoming reactants. The interaction between flame and IRZ may also lead to bifurcations between anchored and lifted regimes [26]. Secondly, irrespective of the injection strategy, swirling flames can exhibit hydrodynamic instabilities such as Precessing Vortex Core that perturb the flow near the injector outlet modifying the flame dynamics [27, 28, 29, 30]. Moreover, experimental studies show that the transition from V-shape to M-shape for CH_4/H_2/air premixed swirling flames can be driven by increased strain resistance due to hydrogen addition [31], confirming results found in [32]. Experimental and numerical works also indicate that flame shape transition can be triggered by heat losses when flames interact with the chamber walls [33, 34].

Both separated injection and swirling motion can be created in coaxial dual-swirl injectors. They represent a potential concept for future H_2-propulsion devices because they guarantee simultaneously flashback resistance and fast mixing [35, 36] to mitigate NO_x. Experimental parametric studies on CH_4 oxy-flames demonstrated that the transition between lifted and attached flames in this kind of systems is piloted by the position of the IRZ with respect to the injector outlet and the lift-off height of the flame depends in the level of internal and external swirl [37]. A similar configuration was recently tested with H_2-enriched mixtures [38] showing that the level of the internal

swirl is a key parameter to control the flame shape, confirming the results provided in [39].

From a numerical perspective, the separated injection strategy leads to flames exhibiting multiple combustion regimes for which the choice of the proper turbulent combustion modelling becomes critical. In this context, a general flamelet transformation was proposed in FPV models to retrieve the local budget of heat source associated with premixed/diffusion combustion [40]. A different method relies on the use of a flame index [41] to discriminate between combustion regimes and apply the corresponding premix/diffusion turbulent combustion model. In this study, this second approach is followed. The modelling relies on the dynamic thickened flame model DTFLES [42] for addressing turbulent/flame interaction in premixed regions, while the resolution of the flame front is ensured for the diffusion zone. This hybrid approach was largely used to describe multi-regime combustion in various spray [43, 44] or gaseous [45] flames and is used here for pure H_2-air gaseous mixtures.

This study deals with LES challenges of such flames. Only few simulations of hydrogen swirling flames exist in literature and mostly for technically premixed combustion, like in [46, 47]. The first objective of this study is to validate the numerical setup used to investigate H_2-air swirled non-premixed flames [38] obtained with the HYdrogen LOw NOx injector (HYLON) developed at IMFT [48]. Second, the flame structure and the flame stabilization mechanisms associated to anchored and lifted H_2-air swirled flames observed experimentally are analyzed. Third, the main aspects governing the unsteady transition from lifted to attached flame are investigated experimentally and numerically.

The rig and the diagnostics are presented in Section 2, while Section 3 describes the numerical setup. In Section 4.1, LES results are validated against experimental measurements. The main characteristics of anchored and lifted flames are illustrated in the rest of the study, where the unsteady transition with lip reattachment of a lifted flame is also discussed.

2. Experimental setup

2.1. Burner geometry

Figure 1(a) shows a schematic description of the HYdrogen LOw NOx injector (HYLON) from IMFT, which was developed to stabilize pure H_2-air swirled flames. It contains two swirling coaxial ducts to inject fuel and oxidizer separately [48]. The annular channel supplies the air mass flow rate with an external diameter d_e = 18 mm. A swirler made of eight cylindrical vanes of diameter d_h = 4 mm, oriented at 42° with respect to the burner radial direction, is embedded in the external passage as shown in Fig. 1(b). The inner injector supplies hydrogen through a d_i = 6 mm diameter tube with 2 mm radial thickness, which contains an axial swirler of helicoidal shape shown in Fig. 1(c). According to [38], the external and the internal swirlers generate a flow with swirl number S_e = 0.65 and S_i = 0.60, respectively. The coaxial burner also features a recess z_i = 4 mm between the lip of the hydrogen injector and the burner backplane that favors mixing of the reactants before burning. The injector feeds a square combustion chamber made of four quartz windows to ensure optical access to the flame region. The chamber is 78 mm wide, 180 mm long and ends with a nozzle that provides a section reduction to avoid reverse flow at the combustor outlet. Detailed information about the injector design can be found in [38].

2.2. Measurements and operating conditions

Mean flame images are recorded with a PIMAX-4 intensified CCD camera equipped with a 105 mm f/4.5 Nikon Rayfact UV-105 Multispectral lens. This camera with an appropriate 308±10 nm narrow band filter ASAHI XHQA310 centered on

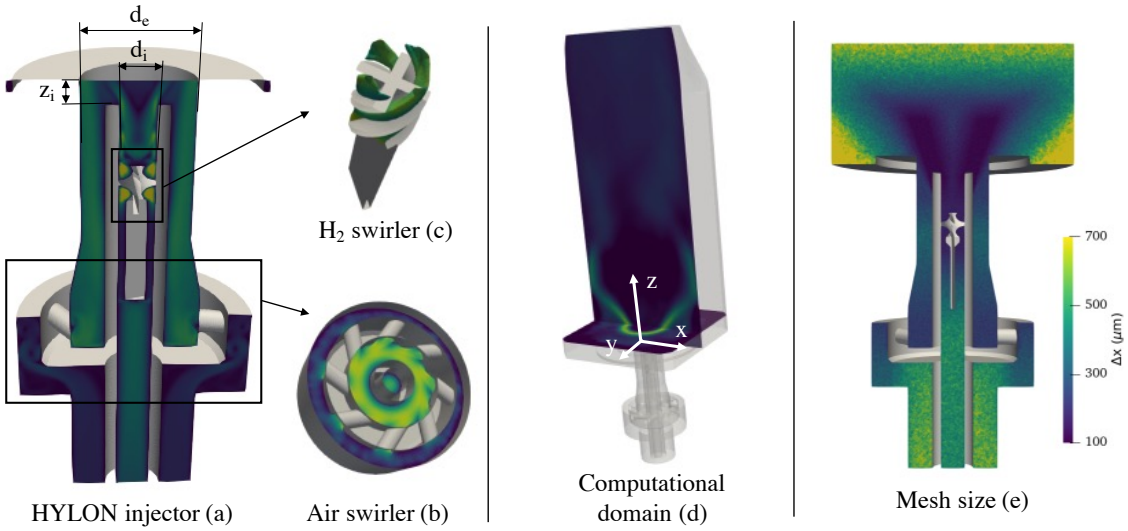

Figure 1: Main components of HYLON injector (a) with air (b) and hydrogen (c) swirlers. Computational domain with the cartesian system of reference (d). Characteristic cell size distribution adopted for spatial discretization (e).

the OH^* peak emission gives indication on both the shape and heat release rate distribution of the flame.

Particle Image Velocimetry (PIV) is performed to characterize the velocity field over a vertical plane in the proximity of the injector outlet either in isothermal (T = 300 K) or reactive conditions. Image pairs are recorded by a 1024×1028 pixels PCO SensiCam CCD Imaging, while in reactive conditions a 2560×2160 pixels LaVision CMOS CLHS camera is employed. In both cases, the cameras are equipped with a Nikkor 105 mm f/2.8G. The laser system consists of a Quantel Big Sky Laser CFR200 with 200 mJ maximum energy per shot at 4/15 Hz repetition rate for cold/hot conditions. The laser passes through a LaVision sheet generator resulting in a relatively thick light sheet of 1.5 mm thickness in the center of the combustion chamber. More than 1000 instantaneous fields are recorded with a LaVision Davis acquisition system to get statistically converged measurements for the mean and rms velocity fluctuations. For cold flow conditions and safety reasons, hydrogen is replaced by air and its mass flow rate in the pilot stream is imposed to conserve the original momentum flux ratio between the internal and external ducts: $J = \rho_e u_e^2/(\rho_i u_i^2)$, where ρ_e/ρ_i and u_e/u_i are the density and the bulk flow velocity in the external/internal duct [37]. Non-reactive and reactive PIV measurements are performed with different seeding particles. For cold flow, oil droplets with a Sauter mean diameter D_{32} = 2 μm are injected both in the external and internal nozzles. In reactive conditions, air and H_2 flows are seeded with Alumina particles AlO_3 of Sauter mean diameter $D_{32} < 1.0$ μm. Measurements are taken on the axial plane zy illustrated in Fig. 1(d) over an interrogation window defined by 2 mm $\leq z \leq$ 32 mm and −25 mm $\leq y \leq$ 25 mm. It was also verified that the azimuthal position of the internal and external swirlers in the computational domain matches the experimental setup in order to maximize the reliability of the comparison between the two.

A thermal characterization of the burner components is also performed for the different operating conditions investigated. For the metallic components a bichromatic infrared FLUKE Endurance series pyrometer is used with spectral response between 1.5 μm and 1.6 μm. It operates between 250 °C and 1200°C, with a relative error equal to ± 0.3% of the measure-

Table 1: Mass flow rates of air and hydrogen, nominal thermal power and global equivalence ratio adopted for the two operating conditions attached (A) and lifted (L).

Case	$\dot{m}_{air}$ [g/s]	$\dot{m}_{H_2}$ [g/s]	$U_b{}^{air}$ [m/s]	$U_b{}^{H2}$ [m/s]	P_{th} [kW]	ϕ_g
A	2.41	0.032	11.4	13.6	3.89	0.45
L	6.03	0.080	28.5	34.0	9.73	0.45

ment. The combustion chamber axial temperature profile is also measured along the centerline of the quartz window with pasted thermocouples. Localized temperature data are also collected on the exhaust nozzle and over the water-cooled burner backplane. Furthermore, a system made of two R-type thermocouples is used to estimate the hot gas temperature at the outlet of the combustion chamber via the reduced radiation error method [49]. Probes are inserted few millimeters below the combustion chamber outlet cross section to estimate the radial temperature profile of the burned gases.

In addition, pressure losses between the injector inlet and ambient are measured for both fuel and oxidizer lines using a differential pressure gauge. Brooks SLA 585x series mass flow controllers are used to regulate hydrogen and air mass flow rates. Fuel and oxidizer are injected at T_u = 298 K.

Two H_2-air flames, one anchored at the H_2 injector lip (flame A) and the other aerodynamically stabilized downstream of the injector (flame L), are investigated. These correspond to the operating conditions detailed in Table 1: the global equivalence ratio is kept constant to $\phi_g = 0.45$, while the total thermal power varies from $P_{th} = 3.89$ kW for flame A to $P_{th} = 9.73$ kW for flame L. The Reynolds number based on the air bulk velocity and on the equivalent hydraulic diameter of the injector annular cross section are 11000 and 28000 for conditions A and L, respectively. Figure 2 shows that flame A is anchored at the H_2 injector lip, while flame L is V-shaped and aerodynamically stabilized downstream of the injector.

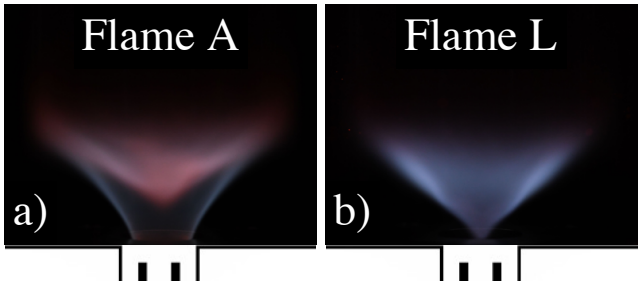

Figure 2: Flame images corresponding to (a) attached flame and (b) lifted flame stabilizations.

3. Numerical framework

3.1. Numerical setup

Numerical simulations are performed using the compressible LES solver AVBP (www.cerfacs.fr/avbp7x/) with the fluid computational domain illustrated in Fig. 1(d). It is delimited at the bottom by the injector inlet and contains the inner swirler, the outer swirler and the entire combustion chamber. The spatial discretization is identical for the two operating conditions investigated and exploits different levels of refinement. Overall it counts 58 M tetrahedral cells, with a minimum characteristic size of 100 µm near the H_2-injector lip and inside the envelope of the regions occupied by non-premixed flame fronts (Fig. 1(e)). The H_2 duct spatial discretization is progressively refined approaching the injector lip. The mesh size distribution in the narrow channels of the helicoidal hydrogen swirler is chosen to capture the strong radial velocity gradients of the hydrogen flow and retrieve the correct velocity field at the injector outlet. A cell size Δx = 200 µm is prescribed for the outer swirler. The heat losses through the walls are modeled for the two flames by imposing the experimental axial temperature profile of the external side of the combustion chamber for operating conditions A and L in Fig. 3. For the combustion chamber, a constant thermal resistance $R = 0.004$ W/m^{2}K is imposed considering the thickness of the quartz windows $l_q = 8$ mm and a thermal conductivity $\lambda_q = 2.07$ W/mK. Thermal radiation through the quartz windows is neglected [50], while the tem-

perature over the combustion chamber backplane that was measured with the pyrometer is fixed to 450 K for both operating conditions. Inlet mass flow rates and outlet pressure are imposed using the NSCBC formalism [51]. The numerical setup relies on a semi-detailed SanDiego chemical mechanism [52] that comprises 9 transported species and 21 reactions.

3.2. An hybrid strategy for mixed turbulent flame

The simulation strategy is designed to capture both premixed and non-premixed combustion regimes expected for conditions *A* and *L*. The perfectly premixed flames are modeled via the DTFLES approach [42] which has been used successfully for many hydrocarbon and hydrogen-blended flames in previous studies, like for instance in [45, 53]. It artificially thickens premixed fronts to allow a sufficient flame resolution relaxing the mesh dimensional constraints, while the flame-turbulence interaction is recovered through a subgrid efficiency model [54]. However, since TFLES is built for premixed flames, it would be inappropriate to use it in case of non-premixed flamelets. Therefore, in these zones, the mesh is fine enough to have a proper resolution of the flame structure and avoid flame thickening. Section 3.3 demonstrates that time-averaged results are independent of the mesh size and that the resolution is adequate. The parameter used to distinguish between the premixed and the diffusion regimes is the normalized Takeno index[41], which is locally updated at each simulation time-step. This is based on the scalar product between the mass fraction gradients of H_2 and O_2. A positive value enables the DTFLES, while a negative one identifies the regions where DTFLES is not suitable for a proper combustion modeling. It is worth mentioning that the aforementioned switch does not impact the momentum equation, which is computed in the entire domain using SIGMA turbulent closure for the subgrid Reynolds stresses [55]. Moreover, the thickening of the flame associated to the DTFLES is modulated by a filter that provides its fast and smooth relaxation outside the premixed zone. This avoids numerical discontinuity at the interface between the two regimes and ensures that the DTFLES does not influence artificially the species diffusion in the resolved regions.

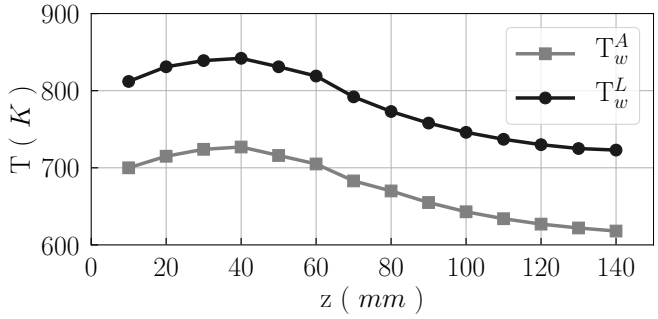

Figure 3: Experimental temperature profiles along the axial direction z of the quartz windows for attached T_w^A and lifted T_w^L operating conditions.

The advantage of the resulting strategy is the possibility to resolve different combustion regimes adopting the same numerical setup and exploiting already established approaches. Its main drawback is the severe grid requirement in the zone of non-premixed flamelets. However, this further computational cost can be limited knowing in advance the regions where non-premixed fronts are expected or making use of mesh refinement techniques [56]. In the present investigation experimental data are used to understand a priori size and shape of the computed flames. Figures 2(a-b), for example, show that reactive fronts of attached/diffusion and lifted/partially-premixed flames lie at different locations, so that the computational grid can be built accordingly.

3.3. Mesh independence of numerical results

To prove that results are mesh-independent a comparison between two grids is proposed in Fig. 4: a reference mesh (Ref) of 58 M tetrahedral elements and a more refined grid (Finer) of roughly 215 M elements. Figure 4(a) shows the cell size (Δx) distribution for the two grids. The flame is visualized by the black contour, which shows the normalized time averaged heat release rate $HRR_{norm} = HRR/HRR_{max} = 0.5$ where the HRR_{max}

is the maximum mean heat release rate. The Ref and the Finer meshes prescribe in this area a cell size Δx = 100 µm and 75 µm, respectively. Overall, Δx in the flame region is reduced by roughly 30% in the second case. In the reference mesh, the grid for the fuel and oxidizer nozzles shows a mesh size between 200 µm and 300 µm, while for the Finer mesh Δx varies between 100 µm and 200 µm. Local refinements are imposed at the injector walls to limit the y^+, which largest values are recorded along the annular external wall of the oxidizer ducts: y^+ is below 15 for Ref mesh and less than 8 for the Finer mesh.

The quality of these grids is compared by computing the anchored flame A which, considering the alignment between isoline of the stoichiometric mixture fraction z_{st} and the heat release rate HRR_{norm} distribution shown in Fig. 4(b), is mainly controlled by diffusion. Data are time-averaged over 30 ms and then spatially averaged along the azimuthal direction before being compared. Figure 4(b) shows the contour map of HRR_{norm} over an axial cut for the Ref mesh (left) and the Finer mesh (right). The isolines of axial velocity $U_z = 0$ and stoichiometric mixture fraction z_{st} are reported in blue and white, respectively. The overall flame size and the global stabilization mechanism are the same irrespective of the grid adopted. The width and the position of the Inner Recirculation Zone (IRZ), which plays a key role in swirling flows, is also unchanged. Figures 5(a-f) display the time-averaged fields of heat release rate (a), gas temperature (b), mixture fraction (c), mean axial velocity (d) and two minor species distributions (e-f) along the radial direction of the burner for three axial coordinates: z = 5 mm, 10 mm and 15 mm. The local heat release rate of the reaction and the distribution of the gas temperature for the two meshes are in good agreement. The consistency of the mixture fraction trend evidences also a coherent spatial distribution of the main species, while the good agreements for Y_H and Y_{HO_2} show that

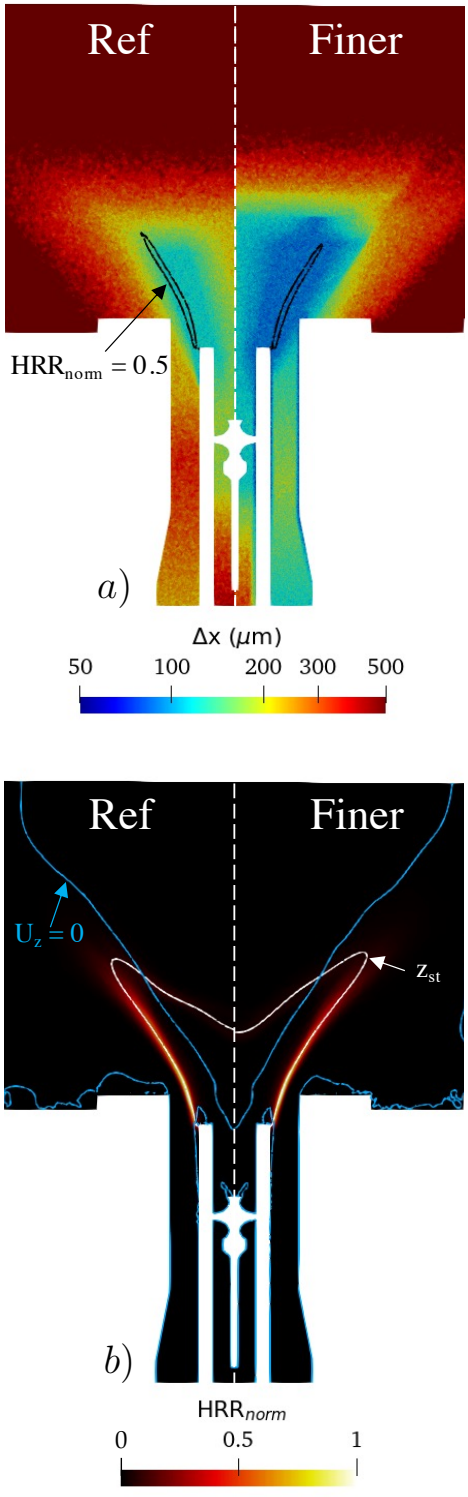

Figure 4: (a) Comparison between the reference (Ref) and the refined (Finer) mesh. The cell size Δx distribution highlights the different grid refinements with superposition of normalized heat release rate isocontour. (b) The time averaged normalized heat release rate HRR_{norm} field for the two grids is displayed with the isolines of axial velocity $U_z = 0$ and the isolines of the stoichiometric mixture fraction z_{st}.

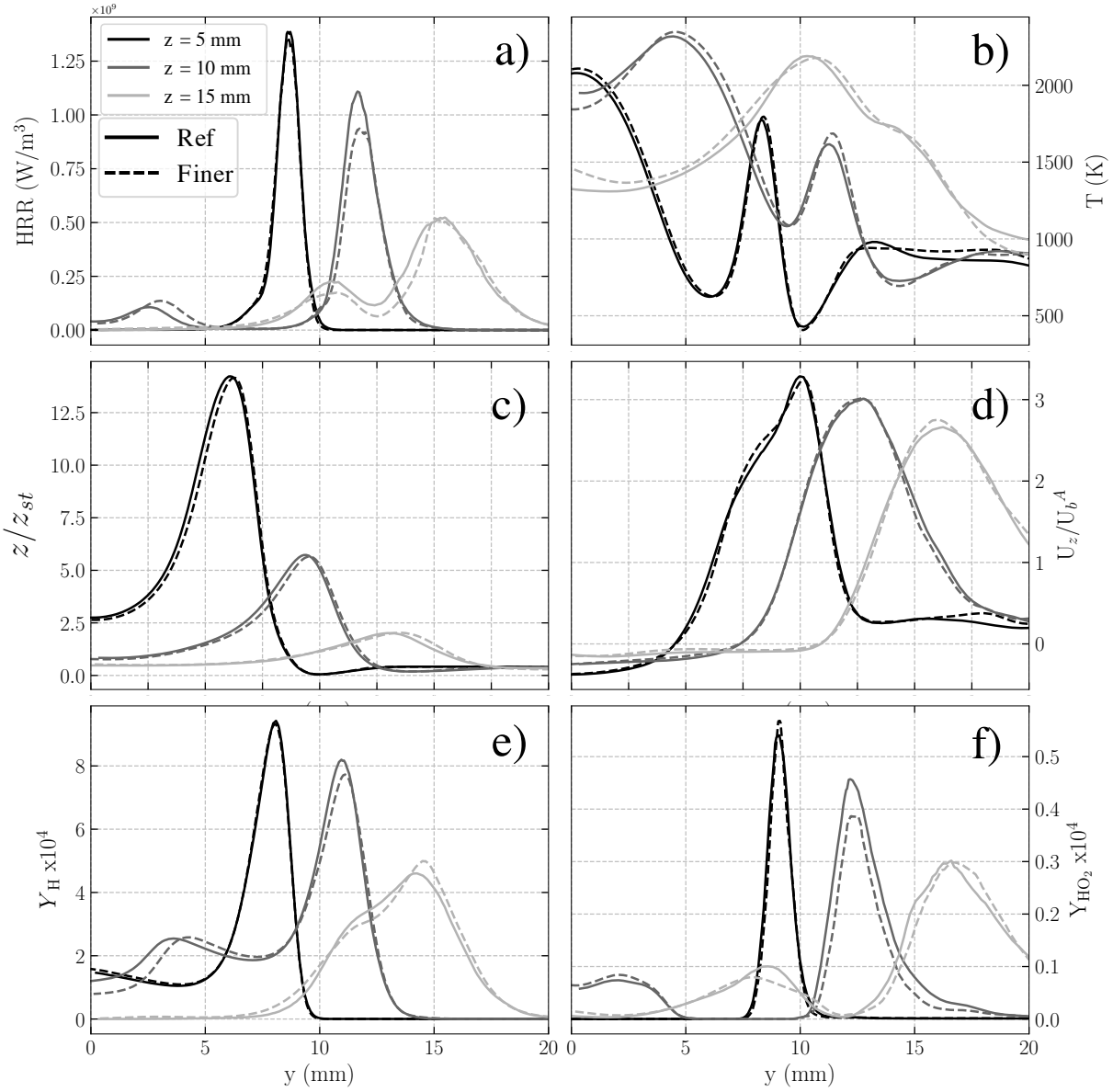

Figure 5: Comparison for the reference (solid) and the finer (dashed) grid in terms of (a) *HRR*, (b) temperature T, (c) mixture fraction z_{st}, (d) mean axial velocity U_z, and mass fractions of Y_H (e) and Y_{HO_2} (f). The variable distributions are presented over the radial direction (y) for three different axial coordinates: z = 5 mm, 10 mm and 15 mm.

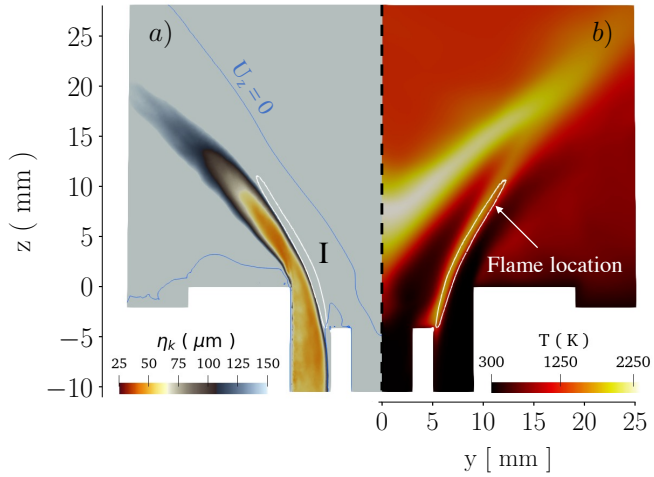

Figure 6: Contour map of the estimated local Kolmogorov scale (a) and the temperature (b) for the anchored flame *A*. The white and the blue iso-lines define the flame location and the limit U_z of the IRZ, respectively.

the structure of the mean flame is correctly captured, independently of the grid. Hence, the resolution of the original mesh is sufficient to produce mesh-independent results on both velocity fields and the mixing process, which are the main parameters driving flame stabilization.

To check the turbulent flow resolution, the Kolmogorov turbulent scale η_k is presented in Fig. 6(a) together with the white line indicating the flame location and $U_z = 0$ isoline in blue delineating the IRZ. The Kolmogorov length scale is evaluated under the simplified hypothesis of isotropic turbulence $\eta_k = L/Re_t^{3/4}$, where L is the diameter of the exit cross section of the injector, while the turbulent Reynolds number $Re_t = u'L/\nu$ is computed knowing the local time-averaged rms velocity u' and the local kinematic viscosity ν[1]. Figure 6(a) illustrates that the smallest turbulent structures in the region of interest range roughly between 50 μm and 75 μm, which are of the order of magnitude of the local cell size and guarantee a reasonable resolution of the flow. Moreover, Fig. 6(b) shows that, because of the penetration of the IRZ inside the injector exit, the H_2 flow is rapidly heated. As result, the viscosity increases and the kinetic energy dissipation limits the energy cascade to eddies that are bigger than η_k. Since it is expected a very little activity at the Kolmogorov scale (see Fig. 5), the resolution of the grid can be considered appropriate.

[1]Considering the good agreement with experimental data shown in Figs. 9 and 10, only the resolved part of u' is retained for the calculation of Re_t

4. Results and discussion

4.1. Velocity fields and pressure losses validation

First, velocity fields obtained with LES are compared to measurements made in isothermal and reactive conditions for the two investigated operating points. LES results and PIV data are gathered on the axial plane zy. Time-averaged solutions are obtained performing LES simulations for an entire flow-through time of the combustion chamber corresponding roughly to 55 ms for the operating condition *A* and 25 ms for *L*. The physical time simulated before collecting statistics corresponds to roughly 150 ms to ensure convergence solutions in both conditions.

Figures 7 and 8 show the comparison between experimental and LES data for non-reacting flows extracted at z = 5 mm and z = 15 mm, respectively. Note that these two heights correspond roughly to the middle and upper parts of the flame. The top graphs in each figure consider the operating condition *A*, while the bottom ones refer to condition *L*. LES are in good agreement with experimental data for both cases. The accurate prediction of the mean axial velocity U_z profile proves that simulations correctly capture the size and the intensity of the IRZ. Moreover, the agreement between experimental and numerical mean radial velocity U_r profiles at both heights indicates that LES accurately predicts the swirling jet opening angle at both operating conditions, thus being representative of the aerodynamics of the injector. In addition to that, the good agreement in terms of rms for both axial U_z and radial U_r components shows that the turbulent velocity fluctuations are also well retrieved by the simulations.

Reactive flows are now considered. Figures 9 and 10 show the comparison between PIV and LES velocity profiles for the reactive flow at $z = 5$ mm and $z = 15$ mm, respectively. Axial and radial velocities are in very good agreement with experiments, both in terms of mean and rms profiles. LES well captures the changes in the velocity field due to the presence of the flame: the peaks of the velocity profiles move outward because of thermal expansion, the width of the IRZ increases and the modulus of the axial velocity inside it reduces. The only marginal difference between experiments and LES is found in Fig. 9 for the rms of the axial U_z and radial U_r velocities near $y = \pm 10$ mm. At $z = 5$ mm this zone corresponds to the location

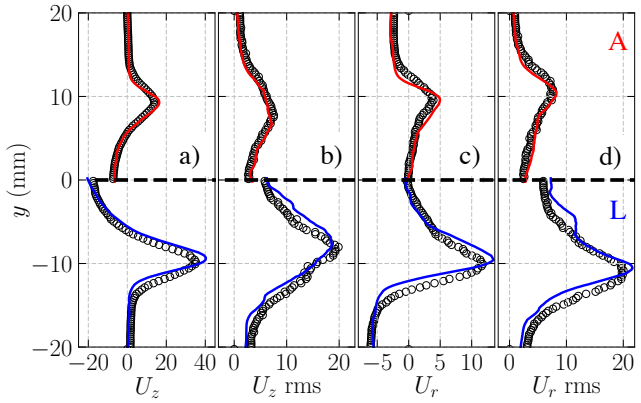

Figure 7: Cold PIV data (symbols) at $z = 5$ mm on the axial plane vs LES results for the mean (a) and rms (b) axial velocity U_z and the mean (c) and rms (d) radial velocity U_r for the operating conditions A (top) and L (bottom). Velocities are in [m/s].

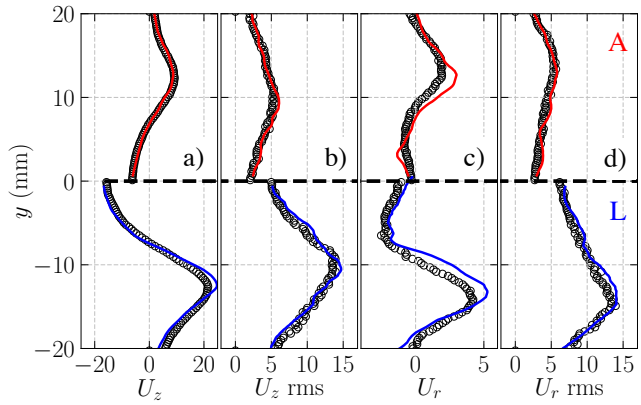

Figure 8: Cold PIV data (symbols) at $z = 15$ mm on the axial plane vs LES results for the mean (a) and rms (b) axial velocity U_z and the mean (c) and rms (d) radial velocity U_r for the operating conditions A (top) and L (bottom). Velocities are in [m/s].

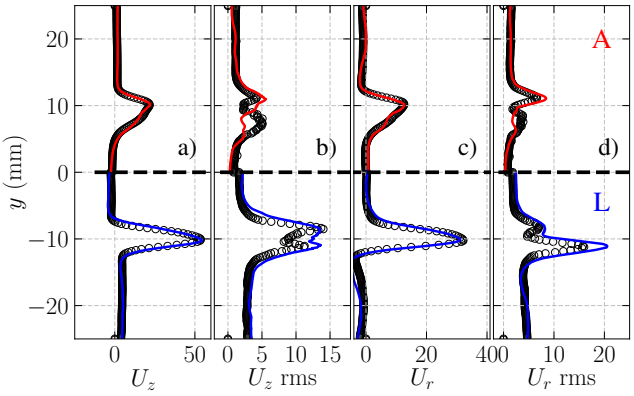

Figure 9: Hot PIV data at $z = 5$ mm on the axial plane vs LES reactive results for the mean (a) and rms (b) axial velocity U_z and the mean (c) and rms (d) radial velocity U_r for operating conditions A (top) and L (bottom). Velocities are in [m/s].

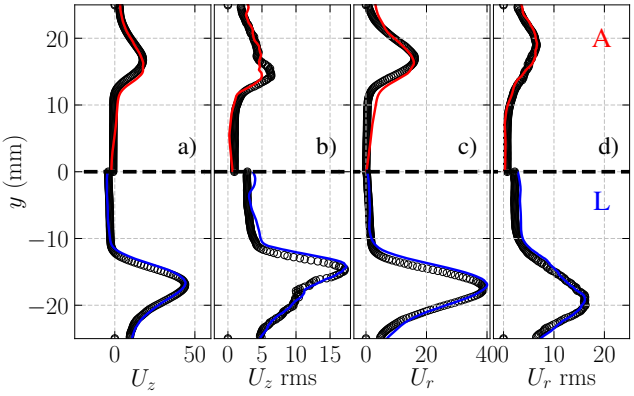

Figure 10: Hot PIV data at $z = 15$ mm on the axial plane vs LES reactive results for the mean (a) and rms (b) axial velocity U_z and the mean (c) and rms (d) radial velocity U_r for operating conditions A (top) and L (bottom). Velocities are in [m/s].

of the outer shear layer which separates the exiting swirling jet from the outer recirculation zone. Figure 4(a) shows that the mesh refinement in this region slightly degrades, justifying this small gap.

Numerical results in terms of injector pressure losses and hot gases outlet temperatures are compared to experimental data in Table 2. The pressure drop $\Delta P_{air}/\Delta P_{H_2}$ represents the differential pressure between the inlet of the air/H_2 injector and ambient. LES data show an overestimation of the absolute pressure losses for both operating conditions A and L. It must be underlined that, even considering the Finer mesh (see Section 3.3) with better refinement of the injector walls, the calcu-

lated pressure losses reduce by only 20 Pa. This is because, in these configurations, most of the pressure losses are due to the swirler [57, 58], suggesting that a further mesh refinement in this zone is needed to improve the prediction of experimental pressure variations. However, considering the agreement between PIV and LES as well as the good qualitative trend of the pressure losses for the two operating conditions, results are considered adequate.

Finally, the comparison between time-averaged outlet gas temperature T_{out} that differ by less than 200 K underlines a satisfactory agreement for both operating conditions, showing that the simulated heat losses are representative of the ones found in the real burner. The small gap between measurements and simulations could be partly due to the assumptions made implementing the reduced radiation error method [49] on experimental data.

Table 2: Measured (*EXP*) and calculated (*LES*) pressures losses for the air injector ΔP_{air} and the H_2 injector ΔP_{H_2}. Mean outlet gas temperature T_{out} for conditions *A* and *L*.

	ΔP_{air} (Pa)	ΔP_{H_2} (Pa)	T_{out} (K)
A_{EXP}	918	165	1138
A_{LES}	1135 (+19%)	215 (+23%)	1010 (−11%)
L_{EXP}	5750	821	1280
L_{LES}	6820 (+16%)	925 (+11%)	1100 (−16%)

4.2. Attached flame (A)

Figure 11 compares the experimental normalized Abel deconvoluted images of the OH* chemiluminescence signal with the LES normalized azimuthal average of the heat release rate HRR_{norm}. Simulations allow to capture the *M*-shape of the attached flame, which can be divided into two main branches. The first one, defined I in Fig. 11, is a vigorous reactive front that develops in the mixing layer between hydrogen and air streams and the second one, named II, that lies downstream of the first one inside the wake of the H_2 injector. According to OH* chemiluminescence measurements, the burning rate in branch II is much weaker than in branch I. For a recess of z_i = 4 mm, the zone between the H_2 injector lip and the chamber backplane is not optically accessible from the present field of view, but LES results in Fig. 11 show that flame *A* is anchored to the injector lip via the branch I which, separating fuel and oxidizer, burns in diffusion-controlled mode. This is corroborated in Fig. 12, which shows the instantaneous fields of the Takeno index (Fig. 12(a)) and the flame thickening distribution (Fig. 12(b)), both conditioned on the same HRR_{norm} threshold. The white contour indicates the instantaneous spatial

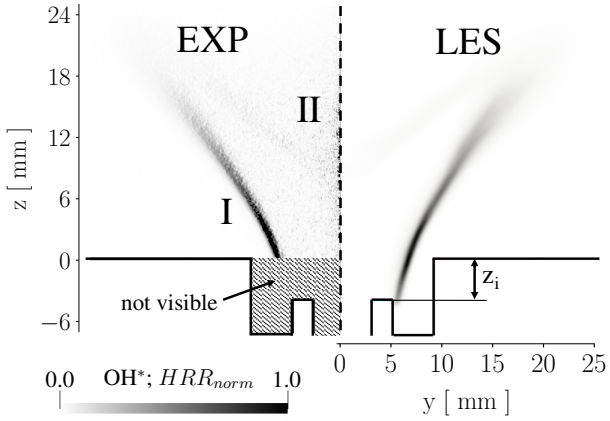

Figure 11: Comparison between experimental mean normalized Abel-deconvoluted OH* chemiluminescence signal (left) and LES normalized time averaged heat release rate distribution HRR_{norm} (right) for flame *A*. The two main flame branches are labelled as I and II.

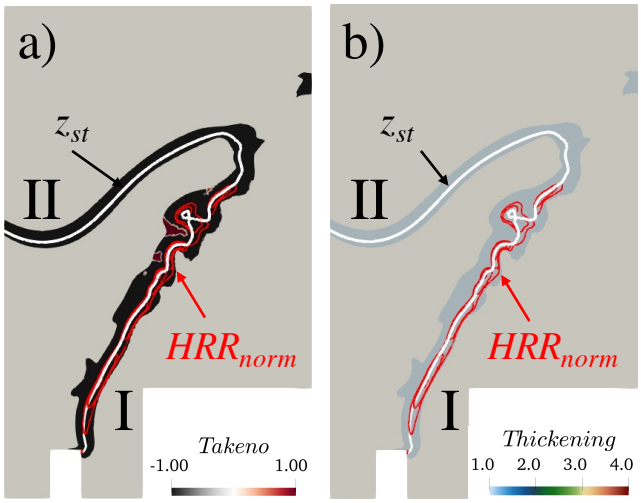

Figure 12: Instantaneous flame structure for flame *A*. Isocontours of normalized heat release rate HRR_{norm} = 0.45, 0.65, 0.80 (solid red) and spatial distribution of stoichiometric mixture fraction z_{st} (solid white) superposed to the Takeno index (a) and thickening factor of the DTFLES model (b).

location of the stoichiometric mixture fraction z_{st}, while the red lines are isocontours of normalized heat release rate HRR_{norm} = 0.45, 0.65 and 0.80. The Takeno index is negative over the entire flame front, meaning that both branches I and II burn in non-premixed mode. Figure 12(b) shows that, as prescribed, flame thickening is not applied for this regime. The flame is entirely resolved by the computational grid and the model is capable of retrieving the global characteristics of the attached configuration.

4.3. Lifted flame (L)

The lifted flame *L* is now discussed. Figure 13 compares the normalized OH* chemiluminescience Abel-deconvoluted signal against the numerical normalized heat release rate HRR_{norm}. The flame stabilization mechanism changes abruptly with respect to the anchored flame. Both experiments and LES show that the location of the maximum mean burning intensity moves downstream and is lifted by roughly 8 mm above the chamber backplane.

Remarkably, Fig. 13 shows that LES also captures the presence of a second weak reaction front II at the flame base that crosses the burner axis. Unlike flame *A*, flame *L* is aerodynamically stabilized in the wake of the hydrogen injector and is not anchored to the burner. The axial distance between the hydrogen injector lip and the main flame front allows a certain degree of mixing between hydrogen and air before burning. The conditioned Takeno index for flame *L* in Fig. 14(a), in fact, indicates that the main reactive front I is partially premixed, since positive and negative values alternate over time and space. On the other side, branch II burns constantly in a diffusion mode as confirmed by both the Takeno index and the alignment between the stoichiometric mixture fraction z_{st} and the heat release rate field.

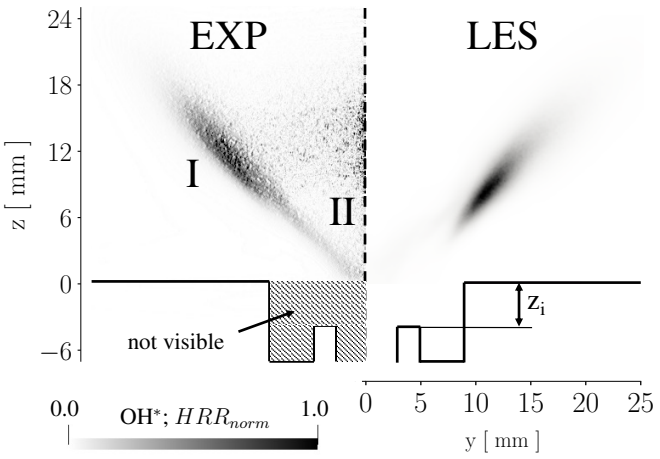

Figure 13: Comparison between experimental mean normalized Abel-deconvoluted OH* chemiluminescence signal (left) and LES normalized time averaged heat release rate distribution HRR_{norm} (right) for flame *L*. The two main flame branches are labelled as I and II.

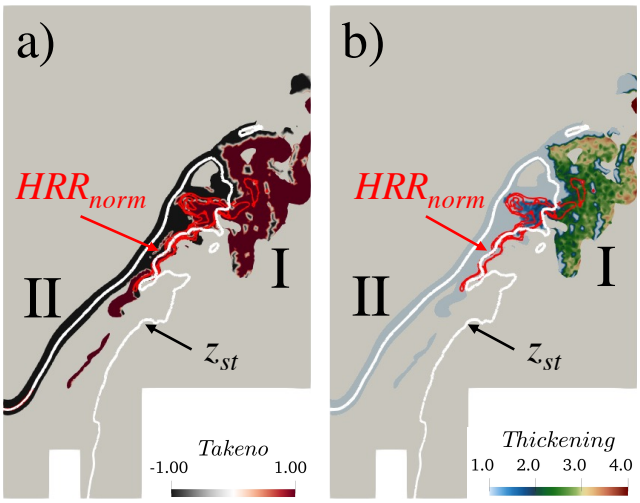

Figure 14: Instantaneous flame structure for flame *L*. Isocontours of normalized heat release rate HRR_{norm} = 0.45, 0.65, 0.80 (solid red) and spatial distribution of stoichiometric mixture fraction z_{st} (solid white) superposed to the Takeno index (a) and to thickening factor of the DTFLES model (b).

4.4. Flame structure comparison

Figure 15 presents the mean absolute velocity field associated to flame *A* (left) and *L* (right). Isolines of U_z = 0 in white highlight the recirculation zones, while the black isocontours of HRR_{norm} = 0.15 enclose the region of the main flame branch I for both operating conditions. Both the attached and lifted flames exhibit a wide IRZ that, favored by the recess z_i = 4 mm, protrudes inside the injector. Figure 15(a) shows that the recirculating mass flow rate creates a blockage at the outlet section of the hydrogen injector, forcing the H_2 stream

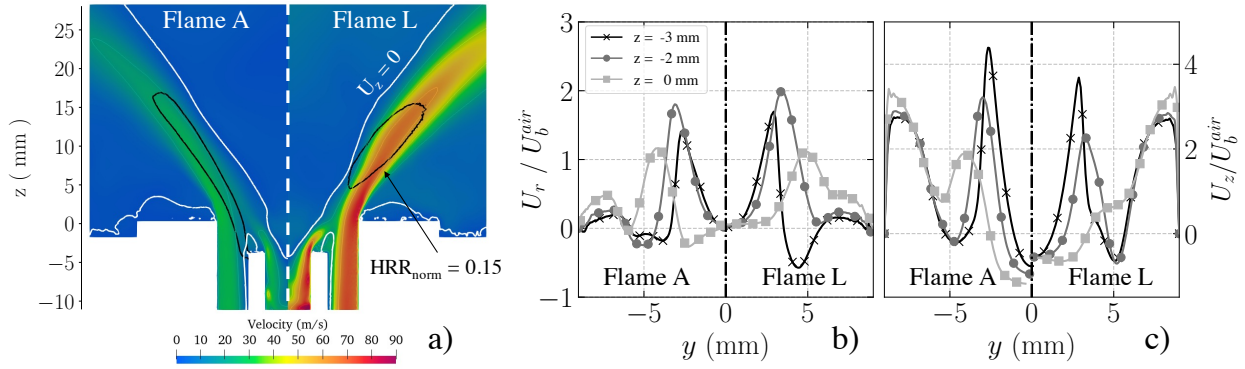

Figure 15: Time averaged distribution of the absolute velocity for the attached (left) and lifted (right) flames (a). The isocontour of $U_z = 0$ delineating recirculation zones is reported in white, while the isoline $HRR_{norm} = 0.15$ defining the main flame branch is depicted in black. The radial and axial normalized velocities are reported in (b) and (c) respectively, showing the velocity distribution in the region of the recess at $z = 0$ mm, $z = -2$ mm and $z = -3$ mm.

to spread radially before reaching the chamber backplane (z = 0). Figures 15(b-c) show the evolution of axial and radial velocity profiles between the outlet section of the H_2 injector and the backplane: z = -3, -2 and 0 mm. The U_z profiles show two distinct peaks for both operating conditions: the internal one is due to the H_2 jet, while the outer one is associated to the lateral air stream. Between these two zones, the local minimum corresponds to the small recirculation zone highlighted in Fig. 15, while the negative U_z velocities near the axis are due to the IRZ that penetrates into the central injector outlet. The mean axial velocity of H_2 reduces along the axial direction due to the radial deviation of the flow. The mean axial velocity of the external air stream, instead, slightly increases before reaching the chamber backplane because the recirculation zone near the lip and the hydrogen flow reduce the cross section available for the annular flow. Despite the larger flow velocities for the lifted flames (Table 1), the overall flow structure is comparable. In both cases the flow squeezes between the IRZ and the recirculation zone above the injector lips, resulting in a peak of U_r at roughly z = -2 mm. Hence, the injector design creates a large recirculation zone that forces the fuel to accelerate radially against the incoming oxidizer. Furthermore, LES allow to calculate the effective swirl number S_f at the injector outlet:

$$S_f = \frac{\int_0^{\frac{d_e}{2}} \rho U_z U_{th}\, r^2 dr}{\frac{d_e}{2} \int_0^{\frac{d_e}{2}} \rho {U_z}^2\, r dr}$$

where $d_e/2$ is the radius of the injector outlet, r the radial direction, ρ the density, U_z the mean axial velocity and U_{th} the mean azimuthal velocity. The calculated value S_f at z = 1 mm is 0.87 for the attached flame A and 0.98 for the lifted flame G. The fact that the velocity fields and the effective swirl numbers are similar for the two flames, suggests that the stabilization regime must depend on the magnitude of the velocity in the vicinity of the injector outlet.

Furthermore, flow separation develops at the top of the H_2 injector lip creating a small recirculation zone that may affect the flame stabilization directly. For example, the left side of Fig. 15(a) shows that the attached flame A anchors preferentially in this low velocity region. The right side of Fig. 15(a) shows that flame L anchors near the inner shear layer between the hot IRZ and the swirling jet of fresh gases. A comparison between the main flame branches I associated to attached and lifted stabilization mechanisms is now provided. Figure 16 shows isocontours of equivalence ratio colored by the normalized heat release rate for flames A and L. The region corresponding to the main heat release rate $HRR_{norm} = 0.15$ is high-

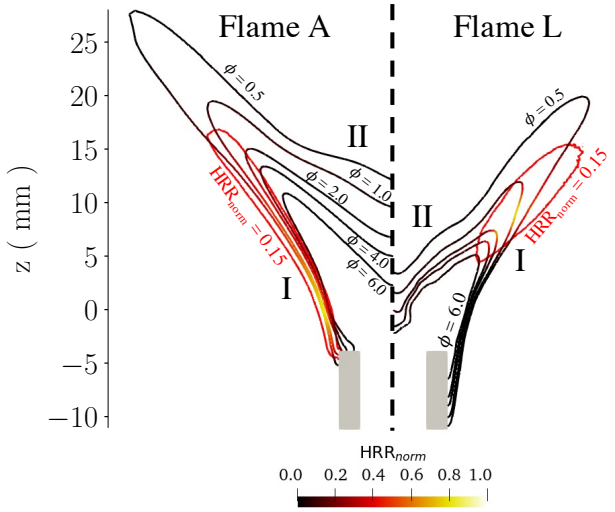

Figure 16: Isocontour of HRR_{norm} defining the main flame branch superposed to the isolines of equivalence ratio to highlight the mixture distribution with respect to the flame location. The two flame branches I and II are highlighted for both types of stabilization.

lighted in red for the two cases. The main branch of the attached flame *A* develops along the stoichiometric mixture fraction z_{st} (see also Fig. 12). In case of flame *L*, instead, Fig. 16 shows that the main flame branch I is characterized by a wide range of mixture compositions. The mean lifted flame is stratified with a local equivalence ratio that gradually decreases from ϕ = 6.0 at the bottom to roughly ϕ = 0.5 at the top. This range is coherently within the flammable limits predicted for freely propagating H_2 air mixtures.

Figure 17 shows the scatter plots of the axial velocity U_z against the coordinate z conditioned by values of HRR_{nrom} > 0.15 for flames *A* and *L*. Data are colored according to the local equivalence ratio ϕ. Figure 17(a) shows that the attached flame is characterized by a wide range of equivalence ratios along its entire length. The upper part of the flame ($z > 0$) is subjected to axial velocities U_z that are much higher than the laminar burning velocity ($U_z >> s_L$), which is generally not compatible with flame stabilization. However, in this case the flame anchors inside the recirculation zone above the H_2 injector lip -4 mm < z < 0 mm remaining far from the low velocity region defined by the IRZ, as shown in Fig. 15(a). Hence, the bottom part of the flame is able to sustain the combustion downstream, even though the flow conditions are less favorable. Figure 17(b) shows the same scatter plot for the lifted flame *L*. In this case, the low velocity region that serves as anchoring point around z = 5 mm lies near the inner shear layer between the swirling jet and the IRZ. Here, reactants are ignited thanks to the recirculation of hot gases and the flame stabilizes between 5 and 10 mm from the backplane. Despite the scatter plot in Fig. 17(b) shows that the upper part of the flame is subjected to high velocity, the flame root serves as ignition source for the rest of the flame front allowing for a stable combustion.

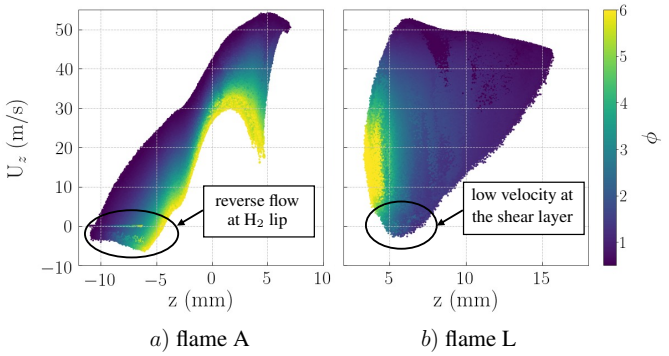

a) flame A *b*) flame L

Figure 17: Scatter plots of axial velocity U_z against the axial coordinate z conditioned by HRR_{norm} > 0.15 and colored according to the local equivalence ratio ϕ for flame *A* (a) and flame *L* (b).

These results suggest that eliminating the small reverse flow near the H_2 lips would favor flame lifting. Furthermore, the fast mixing and the existence of a wide IRZ provided by the specific injector design leads to the presence of the lifted flame.

4.5. Transition dynamics

Previous sections demonstrated that simulations predict correctly two stabilization regimes observed in the experiments for steady state conditions and they allow to investigate their flame structures. This section shows the overall transition from lifted to attached flame, from both experimental and numerical perspectives. Note that, because of hysteresis [59] and variations of the local flow field due to the specific flame position, the passage from lifted to attached flames must not be considered

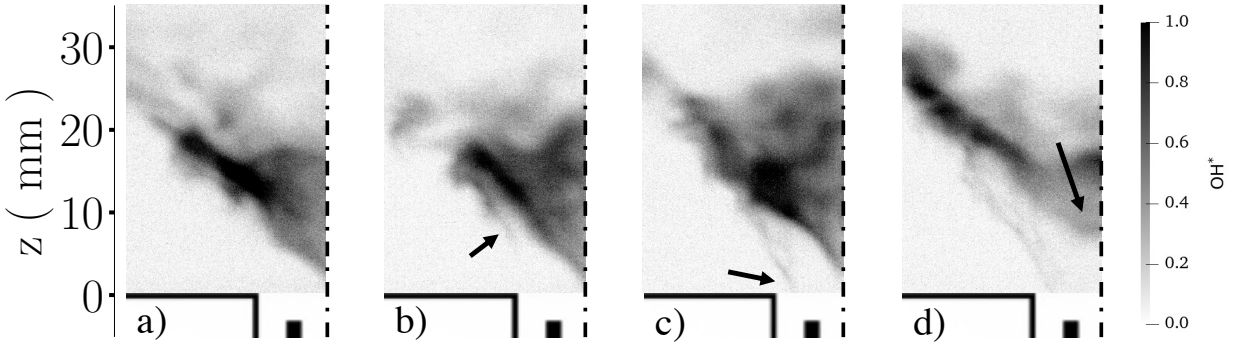

Figure 18: Line of sight integrated images describing the transition to flame lip reattachment: (a) lifted flame, (b) the formation of a lateral branch, (c) propagation of this branch towards the lip and (d) anchored flame.

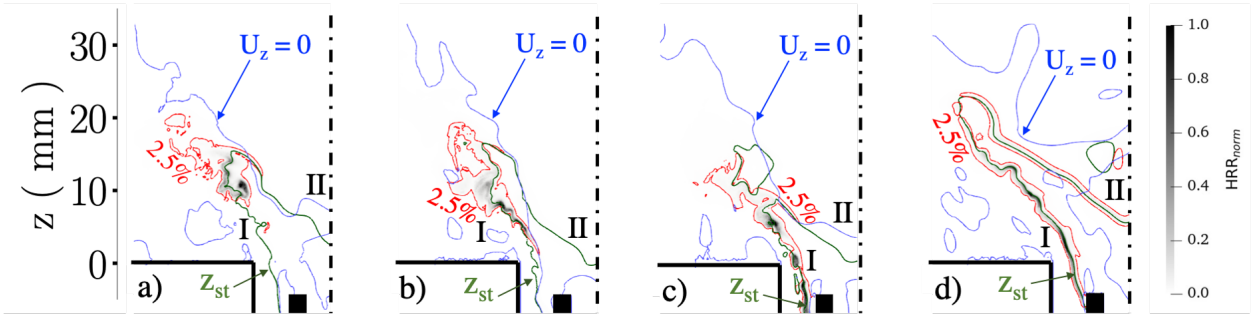

Figure 19: Time evolution in the axial plane of the normalized heat release rate distribution HRR_{norm} with superposition of two isocontours: HRR_{norm} = 0.025 and z_{st} during the transition from lifted L (a) to attached A (d) flame stabilization as consequence of the change of inlet boundary conditions.

as a simple consequence of the two different steady stabilization modes. In fact, the same operating point may lead to different flame characteristics depending on the initial condition. In the laboratory, the change of stabilization from lifted flame (L) is forced by imposing the hydrogen and the air mass flow rates that correspond to the attached one (A). The transition is captured with a Phantom V1612 high speed camera sensible to visible light with an acquisition frequency of 10 kHz. Figure 18 shows 4 instantaneous line of sight integrated images describing the passage from lifted to attached stabilization:

1. Figure 18(a) shows the initial lifted flame. At this point the central part of the flame (II) is close to the injector exit and the main flame region (I) is located on the edge of the IRZ.
2. The second phase is shown in Figure 18(b). The black arrow indicates that the flame re-attachment starts with the formation of a lateral reacting front that propagates upstream.
3. In Fig. 18(c) is shown that this lateral branch propagates upstream towards the injector lip. This evolution is not expected to be axi-symmetric because of local mixture variations and flow inhomogeneities of the turbulent flow. Note that during this phase, the branch II of the flame remains close to the injector outlet.
4. Eventually, when the flame is completely attached around the injector lip, the central diffusion flame II moves downstream along the axial direction recovering the shape of the attached configuration (see Fig. 18(d)).

Numerically, the procedure is mimicked starting from an instantaneous solution of the lifted flame L. The inlet mass flow rate boundary conditions for air and hydrogen are changed at the beginning of the simulation imposing the ones of flame A (see Table 1). Four chronologically-ordered snapshots representative of the computed transition from L to A are illustrated

in Fig. 19. The normalized heat release rate HRR_{norm} is displayed with the superposition of three isocontours corresponding to $HRR_{norm} = 0.025$ in red, z_{st} in green and the isoline $U_z = 0$ in blue. LES recover the global mechanism described in Fig.18. In addition to that, simulations allow to appreciate that between Figs. 19(a) and (c) the flame moves preferentially along the stoichiometric line z_{st}, which corresponds to the location of the most favorable mixture in non-premixed combustion. In these snapshots the position of the isoline $U_z = 0$ is also close to the flame leading point during the entire process. This suggests that the flame propagates along a narrow flammable region under the effect of a low instantaneous axial velocity U_z. Note that, irrespective of the flame position, the stoichiometric line passes near or through the small recirculation zone above the H_2 injector lip. As consequence, during its upstream propagation, the flame is trapped inside this zone, where it eventually stabilizes as in Fig. 19(d). This corroborates the observations made for the steady state case *A*.

These results confirm that the numerical setup can capture the main features of the investigated flame stabilization both for steady injection and transient conditions. A detailed investigation of the transition mechanisms from lifted to attached flames and vice-versa will be the object of future investigations.

5. Conclusion

LES is used to investigate the stabilization mechanisms and the structure of two H_2-air flames obtained experimentally with a dual-swirl coaxial injector (HYLON), in which fuel and air are supplied via a central and an annular duct, respectively. One flame is attached to the injector (*A*) and the other one is aerodynamically stabilized (*L*), hence multiple combustion regimes are involved. Flames feature the same equivalence ratio $\phi_g = 0.45$ but different input thermal powers.

First, the numerical setup is validated against a large set of experimental data including PIV in isothermal and reactive conditions as OH^* flame images, demonstrating that the proposed modeling approach is suitable to compute the non-premixed flames investigated.

The velocity fields for the two operating conditions show the presence of a large IRZ which, penetrating inside the injector, causes a strong radial expansion of the central H_2 swirling jet. Despite the similar flow pattern for the two operating conditions, the flame stabilizations are different. Flame *A* anchors in a low velocity region above the hydrogen injector lip, serving as source of ignition for the rest of the flame branch. In this case the flame evolves in a high velocity region along the mixing layer that separates fuel and oxidizer. This part of the flame burns in diffusion mode along the stoichiometric mixture fraction. The main branch of the lifted flame *L*, instead, stabilizes in the inner shear layer between the IRZ and the exiting hydrogen swirling jet. The flame lift-off permits a degree of mixing that results in a main stratified reaction front characterized by a wide range of equivalence ratios $0.5 < \phi < 6.0$. Both experiments and simulations also show that a second reaction front is found at the interface between the hot recirculating gases and the central H_2 stream. This part of the flame is controlled by diffusion and it only changes in its mean position when passing from lifted to attached stabilization.

Finally, the unsteady transition from lifted to anchored flame is investigated experimentally and numerically. When the flame power is reduced, the lifted flame develops a lateral flame branch that starts propagating towards the injector. LES instantaneous snapshots demonstrate that the flame leading point travels upstream along a trajectory characterized by low axial velocity and near-stoichiometric mixture fractions. Eventually, this front is trapped in a small recirculation zone above the H_2 injector lip and the anchored flame is then retrieved. These observations corroborate the scenario recently proposed in [60] for condi-

tions leading to flame reattachment.

Acknowledgments

This project has received funding from the ERC H2020 Grant Agreement 832248 (SCIROCCO). HPC resources from GENCI (Allocations A0092B10627 and A0112B10157) and PRACE project 2021240098 (WONDER) are also highly acknowledged.

References

[1] M. Fischer, Safety aspects of hydrogen combustion in hydrogen energy systems, Int. J. Hydrog. Energy 11 (1986) 593–601.

[2] M. R. Bothien, A. Ciani, J. P. Wood, G. Fruechtel, Toward decarbonized power generation with gas turbines by using sequential combustion for burning hydrogen, J. Eng. Gas Turbines Power 141 (2019) 121013 (10 pages).

[3] H. Levinsky, Why can't we just burn hydrogen? challenges when changing fuels in an existing infrastructure, Prog. Energy Combust. Sci. 84 (2021) 100907.

[4] A. L. Sánchez, F. A. Williams, Recent advances in understanding of flammability characteristics of hydrogen, Prog. Energy Combust. Sci. 41 (2014) 1–55.

[5] B. Milton, J. Keck, Laminar burning velocities in stoichiometric hydrogen and hydrogen-hydrocarbon gas mixtures, Combust. Flame 58 (1984) 13–22.

[6] F. Halter, C. Chauveau, N. Djebaïli-Chaumeix, I. Gökalp, Characterization of the effects of pressure and hydrogen concentration on laminar burning velocities of methane–hydrogen–air mixtures, Proc. Combust. Inst. 30 (2005) 201–208.

[7] Z. Huang, Y. Zhang, K. Zeng, B. Liu, Q. Wang, D. Jiang, Measurements of laminar burning velocities for natural gas–hydrogen–air mixtures, Combust. Flame 146 (2006) 302–311.

[8] N. Bouvet, F. Halter, C. Chauveau, Y. Yoon, On the effective Lewis number formulations for lean hydrogen/hydrocarbon/air mixtures, Int. J. Hydrog. Energy 38 (2013) 5949–5960.

[9] R. Cheng, A. Oppenheim, Autoignition in methane hydrogen mixtures, Combust. Flame 58 (1984) 125–139.

[10] F. L. Dryer, M. Chaos, Ignition of syngas/air and hydrogen/air mixtures at low temperatures and high pressures: Experimental data interpretation and kinetic modeling implications, Combust. Flame 152 (2008) 293–299.

[11] T. Lieuwen, V. McDonell, E. Petersen, D. Santavicca, Fuel flexibility influences on premixed combustor blowout, flashback, autoignition, and stability, J. Eng. Gas Turbines Power 130 (2008) 011506 (10 pages).

[12] D. Ebi, N. T. Clemens, Experimental investigation of upstream flame propagation during boundary layer flashback of swirl flames, Combust. Flame 168 (2016) 39–52.

[13] W. M. Pitts, Assessment of theories for the behavior and blowout of lifted turbulent jet diffusion flames, Symposium (International) on Combustion 22 (1989) 809–816.

[14] K. M. Lyons, Toward an understanding of the stabilization mechanisms of lifted turbulent jet flames: experiments, Prog. Energy Combust. Sci. 33 (2007) 211–231.

[15] L. Vanquickenborne, A. van Tiggelen, The stabilization mechanism of lifted diffusion flames, Combust. Flame 10 (1966) 59–69.

[16] R. Günther, K. Horch, B. Lenze, The stabilization mechanism of free jet diffusion flames, in: First Specialists Meeting (International) of the Combustion Institute, 1981, pp. 20–24.

[17] N. Peters, F. A. Williams, Liftoff characteristics of turbulent jet diffusion flames, AIAA J. 21 (1983) 423–429.

[18] S. Byggstøyl, B. Magnussen, Turbulent shear flows 4, Springer-Verlag, New York 381 (1985).

[19] A. Upatnieks, J. F. Driscoll, C. C. Rasmussen, S. L. Ceccio, Liftoff of turbulent jet flames—assessment of edge flame and other concepts using cinema-PIV, Combust. Flame 138 (2004) 259–272.

[20] G. R. Ruetsch, L. Vervisch, A. Liñán, Effects of heat release on triple flames, Phys. Fluids 7 (1995) 1447–1454.

[21] L. Muñiz, M. Mungal, Instantaneous flame-stabilization velocities in lifted-jet diffusion flames, Combust. Flame 111 (1997) 16–31.

[22] R. Schefer, P. Goix, Mechanism of flame stabilization in turbulent, lifted-jet flames, Combust. Flame 112 (1998) 559–574.

[23] S. Meares, A. R. Masri, A modified piloted burner for stabilizing turbulent flames of inhomogeneous mixtures, Combust. Flame 161 (2014) 484–495.

[24] T. F. Guiberti, W. R. Boyette, Y. Krishna, W. L. Roberts, A. R. Masri, G. Magnotti, Assessment of the stabilization mechanisms of turbulent lifted jet flames at elevated pressure using combined 2-D diagnostics, Combust. Flame 214 (2020) 323–335.

[25] S. Candel, D. Durox, T. Schuller, J.-F. Bourgouin, J. P. Moeck, Dynamics of swirling flames, Annu. Rev. Fluid Mech. 46 (2014) 147–173.

[26] M. Tummers, A. Hübner, E. van Veen, K. Hanjalić, T. van der Meer, Hysteresis and transition in swirling nonpremixed flames, Combust. Flame 156 (2009) 447–459.

[27] M. Stöhr, I. Boxx, C. Carter, W. Meier, Dynamics of lean blowout of a

swirl-stabilized flame in a gas turbine model combustor, Proc. Combust. Inst. 33 (2011) 2953–2960.

[28] D. Galley, S. Ducruix, F. Lacas, D. Veynante, Mixing and stabilization study of a partially premixed swirling flame using laser induced fluorescence, Combust. Flame 158 (2011) 155–171.

[29] Z. Yin, P. Nau, W. Meier, Responses of combustor surface temperature to flame shape transitions in a turbulent bi-stable swirl flame, Exp. Therm. Fluid Sci. 82 (2017) 50–57.

[30] Q. An, A. M. Steinberg, The role of strain rate, local extinction, and hydrodynamic instability on transition between attached and lifted swirl flames, Combust. Flame 199 (2019) 267–278.

[31] T. Guiberti, D. Durox, P. Scouflaire, T. Schuller, Impact of heat loss and hydrogen enrichment on the shape of confined swirling flames, Proc. Combust. Inst. 35 (2015) 1385–1392.

[32] D. Wicksall, A. Agrawal, R. Schefer, J. Keller, The interaction of flame and flow field in a lean premixed swirl-stabilized combustor operated on H_2/CH_4/air, Proc. Combust. Inst. 30 (2005) 2875–2883.

[33] T. F. Guiberti, D. Durox, L. Zimmer, T. Schuller, Analysis of topology transitions of swirl flames interacting with the combustor side wall, Combust. Flame 162 (2015) 4342–4357.

[34] R. Mercier, T. Guiberti, A. Chatelier, D. Durox, O. Gicquel, N. Darabiha, T. Schuller, B. Fiorina, Experimental and numerical investigation of the influence of thermal boundary conditions on premixed swirling flame stabilization, Combust. Flame 171 (2016) 42–58.

[35] V. Tangirala, R. H. Chen, J. F. Driscoll, Effect of heat release and swirl on the recirculation within swirl-stabilized flames, Combust. Sci. Technol. 51 (1987) 75–95.

[36] R.-H. Chen, J. F. Driscoll, The role of the recirculation vortex in improving fuel-air mixing within swirling flames, Symposium (International) on Combustion 22 (1989) 531–540.

[37] A. Degeneve, R. Vicquelin, C. Mirat, J. Caudal, T. Schuller, Impact of co- and counter-swirl on flow recirculation and liftoff of non-premixed oxy-flames above coaxial injectors, Proc. Combust. Inst. 38 (2021) 5501–5508.

[38] S. Marragou, H. Magnes, T. Poinsot, L. Selle, T. Schuller, Stabilization regimes and pollutant emissions from a dual fuel CH_4/H_2 and dual swirl low nox burner, Int. J. Hydrog. Energy 47 (2022) 19275–19288.

[39] S. Yuasa, Effects of swirl on the stability of jet diffusion flames, Combust. Flame 66 (1986) 181–192.

[40] E. Knudsen, H. Pitsch, A general flamelet transformation useful for distinguishing between premixed and non-premixed modes of combustion, Combust. Flame 156 (2009) 678–696.

[41] H. Yamashita, M. Shimada, T. Takeno, A numerical study on flame stability at the transition point of jet diffusion flames, Proc. Combust. Inst. 26 (1996) 27–34.

[42] J. P. Legier, T. Poinsot, D. Veynante, Dynamically thickened flame LES model for premixed and non-premixed turbulent combustion, Proceedings of the Summer Program, Centre for Turbulence Research (2000) 157–168.

[43] D. Paulhiac, B. Cuenot, E. Riber, L. Esclapez, S. Richard, Analysis of the spray flame structure in a lab-scale burner using large eddy simulation and discrete particle simulation, Combust. Flame 212 (2020) 25–38.

[44] E. Lo Schiavo, D. Laera, E. Riber, L. Gicquel, T. Poinsot, Effects of liquid fuel/wall interaction on thermoacoustic instabilities in swirling spray flames, Combust. Flame 219 (2020) 86–101.

[45] D. Laera, P. Agostinelli, L. Selle, Q. Cazères, G. Oztarlik, T. Schuller, L. Gicquel, T. Poinsot, Stabilization mechanisms of CH_4 premixed swirled flame enriched with a non-premixed hydrogen injection, Proc. Combust. Inst. 38 (2021) 6355–6363.

[46] D. Mira, O. Lehmkuhl, A. Both, P. Stathopoulos, T. Tanneberger, T. G. Reichel, C. O. Paschereit, M. Vázquez, G. Houzeaux, Numerical characterization of a premixed hydrogen flame under conditions close to flashback, Flow Turbul. Combust. 104 (2020) 479–507.

[47] T. Capurso, D. Laera, E. Riber, B. Cuenot, NO_x pathways in lean technically premixed swirling H_2-air turbulent flame, Combust. Flame (2022) Accepted.

[48] S. Richard, C. Viguier, S. Marragou, T. Schuller, Dispositif d'injection de dihydrogène et d'air (FR Patent No FR2111267), Institut National de la Propriété Industrielle, 2021.

[49] S. Brohez, C. Delvosalle, G. Marlair, A two-thermocouples probe for radiation corrections of measured temperatures in compartment fires, Fire Saf. J. 39 (2004) 399–411.

[50] A. Degenève, P. Jourdaine, C. Mirat, J. Caudal, R. Vicquelin, T. Schuller, Analysis of wall temperature and heat flux distributions in a swirled combustor powered by a methane-air and a CO_2-diluted oxyflame, Fuel 236 (2019) 1540–1547.

[51] T. Poinsot, S. Lele, Boundary conditions for direct simulations of compressible viscous flows, J. Comput. Phys. 101 (1992) 104–129.

[52] P. Saxena, F. Williams, Testing a small detailed chemical-kinetic mechanism for the combustion of hydrogen and carbon monoxide, Combust. Flame 145 (2006) 316–323.

[53] P. Agostinelli, D. Laera, I. Chterev, I. Boxx, L. Gicquel, T. Poinsot, On the impact of H_2-enrichment on flame structure and combustion dynamics of a lean partially-premixed turbulent swirling flame, Combust. Flame 241 (2022) 112120.

[54] F. Charlette, C. Meneveau, D. Veynante, A power-law flame wrinkling

model for les of premixed turbulent combustion part i: non-dynamic formulation and initial tests, Combust. Flame 131 (2002) 159–180.

[55] F. Nicoud, H. B. Toda, O. Cabrit, S. Bose, J. Lee, Using singular values to build a subgrid-scale model for large eddy simulations, Phys. Fluids 23 (2011) 085106.

[56] P. Agostinelli, B. Rochette, D. Laera, J. Dombard, B. Cuenot, L. Gicquel, Static mesh adaptation for reliable large eddy simulation of turbulent reacting flows, Phys. Fluids 33 (2021) 035141.

[57] G. Daviller, M. Brebion, P. Xavier, G. Staffelbach, J.-D. Müller, T. Poinsot, A mesh adaptation strategy to predict pressure losses in les of swirled flows, Flow Turbul. Combust. 99 (2017) 93–118.

[58] A. Aniello, D. Schuster, P. Werner, J. Boussuge, M. Gatti, C. Mirat, L. Selle, T. Schuller, T. Poinsot, U. Rüde, Comparison of a finite volume and two lattice boltzmann solvers for swirled confined flows, Comput. Fluids 241 (2022) 105463.

[59] S. R. Gollahalli, ö. Savaş, R. Huang, J. L. Rodriquez Azara, Structure of attached and lifted gas jet flames in hysteresis region, Proc. Combust. Inst. 21 (1988) 1463–1471.

[60] S. Marragou, H. Magnes, A. Aniello, L. Selle, T. Poinsot, T. Schuller, Experimental analysis and theoretical lift-off criterion for H_2/air flames stabilized on a dual swirl injector, Proc. Combust. Inst. (2022). doi:https://doi.org/10.1016/j.proci.2022.07.255.